Optimizing Wing Structural Design: Evaluating Infill Geometry and Print Orientation on the Structural Integrity of PLA Components

Xiaofeng Tan[1], MyHanh C. Lee[2], Bryan I. Mendoza[3], Banu T. Seelam[4],
Jeffrey G. Marchetta[5], and Daniel V. Foti[6]
The University of Memphis, Tennessee, 38152, United States

In the AIAA Design, Build, Fly (DBF) Competition, material selection is a critical engineering consideration due to the need for balancing structural performance with logistical constraints. This study examines the 3D-printed polylactic acid (PLA) wing ribs to determine the optimal infill pattern and percentage based on weight, time, and cost. PLA is selected due to supply limitations and unavailability of CNC machining and ensures timely aircraft production by allowing parts to be manufactured on demand. Testing for the 3D-printed rib sections includes the grid, honeycomb, and gyroid patterns with 10%, 15%, and 20% densities. The quarter chord is subjected to a load force to examine how the worst-case scenario load, applied to the aerodynamic center, affects the structure of the rib. These findings are used to guide the selection of future PLA rib designs to support the construction of a functional flying aircraft.

I. Nomenclature

L	=	Lift force [lb]
$L'_{Schrenk}$	=	Spanwise lift distribution [lb/in]
$L'_{elliptical}$	=	Lift distribution across the span [lb/in]
$L'_{planform}$	=	Wing planform distribution [lb/in]
W	=	Load [lb]
y	=	Spanwise location [in]
b	=	Wingspan [in]
λ	=	Taper ratio
A	=	Area [in^2]
$\bar{z}$	=	Neutral axis [in]
I	=	Area moment of inertia [in^4]
Z_u	=	Upper layer of the airfoil
Z_l	=	Lower layer of the airfoil
M_{max}	=	Maximum moment [lb·in]
σ	=	Bending Stress [lb/in^2]
c	=	Distance from the centroidal neutral axis to the extreme outer fiber [in]
C_l	=	Coefficient of lift
V	=	Relative velocity (true airspeed) [ft/s]
ρ	=	Local density of air [lbm/ft^3]

[1]Undergraduate Student, Department of Mechanical Engineering, AIAA Student Member Number 1864329
[2]Undergraduate Student, Department of Mechanical Engineering, AIAA Student Member Number 1399932
[3]Undergraduate Student, Department of Mechanical Engineering, AIAA Student Member Number 1400317
[4]Undergraduate Student, Department of Mechanical Engineering, AIAA Student Member Number 1422257
[5]Professor and Undergraduate Coordinator, Department of Mechanical Engineering, AIAA Associate Fellow
[6]Associate Professor and Graduate Coordinator, Department of Mechanical Engineering, AIAA Member

II. Introduction

Unmanned Aerial Vehicles (UAV) are remote-controlled flight systems that operate without a human pilot on board. In UAV design, structural stability is balanced with minimal weight required to achieve aerodynamic efficiency. Small UAV performance is highly sensitive to weight; therefore, reducing structural weight allows greater lift efficiency, lowers required thrust, and minimizes drag [1].

The key aspects of UAV design serve as a guide for aligning aircraft design decisions with the Design, Build, Fly (DBF) competition's mission and dimensional constraints. The objective for the 2025-2026 DBF competition is to design, build, and test an electric-powered, remote-controlled bush plane capable of performing charter missions and towing a deployable banner. The aircraft must complete three missions: one without payload, the second with passengers and cargo, and the third involving the remote deployment of a banner. The plane is required to fly three laps within five minutes for each mission. The fuselage must contain at least one passenger compartment and one cargo compartment, and the wingspan may not exceed five feet. These mission constraints place significant emphasis on structural efficiency, weight reduction, and reliable manufacturability [2].

During the transition from the preliminary design to the detailed design, the team identified key challenges that drove design modifications. The first iteration involved a material selection change for the airfoil ribs. Material sourcing constraints and limited access to a CNC machine represented the first challenges the team encountered. The team transitioned from balsa wood to polylactic acid (PLA) based on structural, manufacturing, and consistency trade-offs. This transition motivated the use of additive manufacturing, such as 3D printing, which will allow precise control over internal geometry and repeatable part production [3]. This decision ultimately led the team to research PLA in depth as the team became interested in optimizing infill percentages and patterns to achieve the best balance between lightweight performance, manufacturability, and cost. To evaluate these configurations, a simple bending test was selected as the primary experimental method to compare structural strength and flexibility across different printed samples.

III. Wing Rib and Additive Manufacturing Parameters

A. Rib Model

The team evaluated the requirements for the 2026 DBF competition to determine the best airfoil for the wing. The plane must carry cargo, deploy/release a banner, and sustain the weight of its components during flight missions. With this, the team sought out an airfoil possessing a high C_l throughout a range of angles of attack (α) and with gradual and forgiving stall characteristics. Additionally, an airfoil that was simple to work with and manufacture was considered because of the lack of resources during the time of planning. Looking through an airfoil database, the NACA 2412 was chosen. The NACA 2412 airfoil has a $C_l \approx 0.25\text{-}1.45$ throughout angles of 0° to 15° respectively [5]. Here, we choose an incident angle of 5° for the calculations and obtain the corresponding C_l of 0.803 with respect to the Reynolds number, Re = 242,100, obtained from an approximate speed of 25.1 mph or 36.8 ft/s.

$$L = \frac{1}{2} C_l V^2 \rho A_s \tag{1}$$

The lifting force of 5.34 lb was determined using Eq. 1. Assuming the total weight of the plane is 4.75 lb, calculations for a 4:1 aspect ratio give the plane the wing dimensions of 4 ft x 1.055 ft. This gives the plane a sufficient lift-weight ratio of 1.125. A positive ratio results in increased range and improved fuel economy. To further improve the ratio, the weight can also be reduced. Since a solid rib increases the overall weight of the plane, holes can be added to the rib to reduce weight while maintaining structural integrity [4]. Notches and holes also serve as necessary connection points for the stringers and spars, respectively.

B. Material and Printing Parameters

Polylactic Acid (PLA) was selected for the airfoil ribs because it has several advantages. It is a biodegradable thermoplastic commonly used in 3D printing. Table 1 shows the physical properties of PLA [6]. PLA has a density of 0.043 lb./in^3 at 21.5˚C [6]. It is lightweight and effective for 3D printing applications. Slicer software, such as Ultimaker Cura or PrusaSlicer, default to PLA over other materials due to its ease of use, low melting temperature, optional heated bed requirement, and low warping, oozing, and clogging [7]. The Vicat Softening Temperature (VST) indicates the maximum temperature at which the material can maintain stability under load. The VST for PLA is 64.2 ˚C, meaning it can retain its structural stability and shape without deformation below this temperature. The melt index measures the ease of extrusion of PLA in its molten state. Its melt index of 0.0198 lb/10 min at 210 °C indicates that its flow characteristics are moderate: the higher the Melt Index of the material, the better flowability [8]. In addition, its relatively low melting temperature of 148 ˚C supports efficient extrusion and layer-by-layer placement during printing, and higher feed rates because the nozzle reaches required temperature quickly. The physical properties of PLA provide dimensional stability and controlled extrusions supporting suitability for fabrication.

Table 1 Physical Properties of Polylactic Acid (PLA)

Property	*Testing Method*	*Typical Value*	*Unit*
Density at 21.5˚C	ISO 1183, GB/T 1033	0.043	lb./in^3
Vicat Softening Temperature	ISO 1183, GB/T 1033	64.2	˚C
Melt Index	210 °C, 2.15 kg	0.0198	lb/10 min
Melting Temperature	DSC, 10°C/min	148	˚C

The mechanical properties of PLA, shown in Table 2, indicate that it is stiff, moderately strong, and brittle with low ductility, while providing adequate bending resistance for lightweight 3D-printed components [6]. The mechanical properties of PLA demonstrate directional dependence as reflected in the higher tensile strength (6.83 ksi) and stiffness (383.04 ksi) in the X-Y plane compared to the Z-axis (5.64 ksi). PLA's bending modulus (475.58 ksi) and bending strength (12.31 ksi) indicate that it can resist moderate flexural loads but is stiff and brittle due to its low elongation at break (5%). Based on these properties, the airfoil ribs were printed so that the primary stresses align with the X-Y layers. Printing the ribs flat, versus vertically, maximizes the strength of the rib with thicker walls, reduces brittleness, and eliminates the need to print supports for the specimen which adds to the overall print time. These behaviors of the 3D-printed PLA demonstrate the influence of PLA layer orientation and interlayer bonding on mechanical performance [9]. Overall, PLA provides sufficient strength and stiffness, good printability, and low density for airfoil ribs when the print orientation is selected to maximize strength and reduce brittleness in the X-Y plane. Different infill patterns and densities were tested to evaluate the effectiveness of material distribution and internal geometry on mechanical performance.

Table 2 Mechanical Properties of Polylactic Acid (PLA)

Property	*Testing Method*	*Typical Value*	*Unit*
Young's Modulus (X-Y)	ISO 527, GB/T 1040	383.04 ± 47.57	ksi
Tensile Strength (X-Y)	ISO 527, GB/T 1040	6.83 ± 0.17	ksi
Tensile Strength (Z)	ISO 527, GB/T 1040	5.64 ± 0.07	ksi
Elongation at Break (X-Y)	ISO 527, GB/T 1040	5.1 ± 0.0	%
Bending Modulus (X-Y)	ISO 178, GB/T 9341	475.58 ± 19.44	ksi
Bending Strength (X-Y)	ISO 178, GB/T 9341	12.31 ± 0.45	ksi
Notched Charpy Impact Strength (X-Y)	ISO 179, GB/T 1043	0.27 ± 0.03	BTU/ft^2

All testing specimens were printed under the following conditions: nozzle temperature = 205 °C, printing speed = 60 mm/s, build plate temperature = 40 °C, infill = 100%. All specimens were conditioned at room temperature for 24h prior to testing.

The Anycubic Kobra Max 3D Printer was used to fabricate the airfoil ribs for testing with Grid, Gyroid, and Honeycomb infill patterns at densities of 10%, 15%, and 20% (Fig. 1) [10]. For each infill and density combination, three samples were printed to verify experimental and results consistency. The Ultimaker Cura slicer was used to prepare the Grid and Gyroid infill patterns, whereas the PrucerSlicer was used for the Honeycomb as this pattern is an option within Cura. The Grid pattern at 15% infill is the default setting and was therefore selected as the baseline configuration. The 10% and 20% infill densities were included to investigate the effect of material distribution below and above the default setting. The Grid forms a pattern of squares by creating two perpendicular lines, making it a strong pattern [11]. The Gyroid was selected for testing because it is a unique pattern that is flexible due to its wavy patterns that alternate directions [12]. The Honeycomb was selected because it consists of a hexagonal pattern that provides improved mechanical strength [12]. The geometry of the Honeycomb distributes loads efficiently and in multiple directions [13]. This provides higher stiffness and better energy absorption. Table 3 provides an overview of the Anycubic Kobra Max 3D Printer settings and infill patterns used in this research.

Table 3 Parameters of the Anycubic Kobra Max 3D Printer Tested with 3D Printed Specimen of 100% Infill

Material/Filament Information		**Print Settings**	
Material Type	PLA	Layer Height (in.)	0.0079
Filament Diameter (in.)	0.07	Print Speed (in./s)	3.15
Color	Black	Infill %	10, 15, 20
Temperature Settings		Infill Pattern	Grid, Gyroid, Honeycomb
Nozzle Temperature (˚C)	190	Shell Thickness (in.)	0.047
Bed Temperature (˚C)	60	No. of Top/Bottom Layers	6/6
Cooling Fan Speed (%)	100	Initial Height Layer (in.)	0.047
Retraction Settings		Initial Layer Speed (in.)	3.14
Retraction Distance (in.)	0.24	**Adhesion Supports**	
Retraction Speed (in./s)	1.57	Build Plate Adhesion	Brim
Z-Hop Height (in.)	0.003	Support Structures	None
Printing		**Software**	
Build Size (in.)	15.74x15.75x17.12	Slicing Software	Cura, Prusa
Nozzle Diameter (in.)	0.016	Software Input Format	. STL

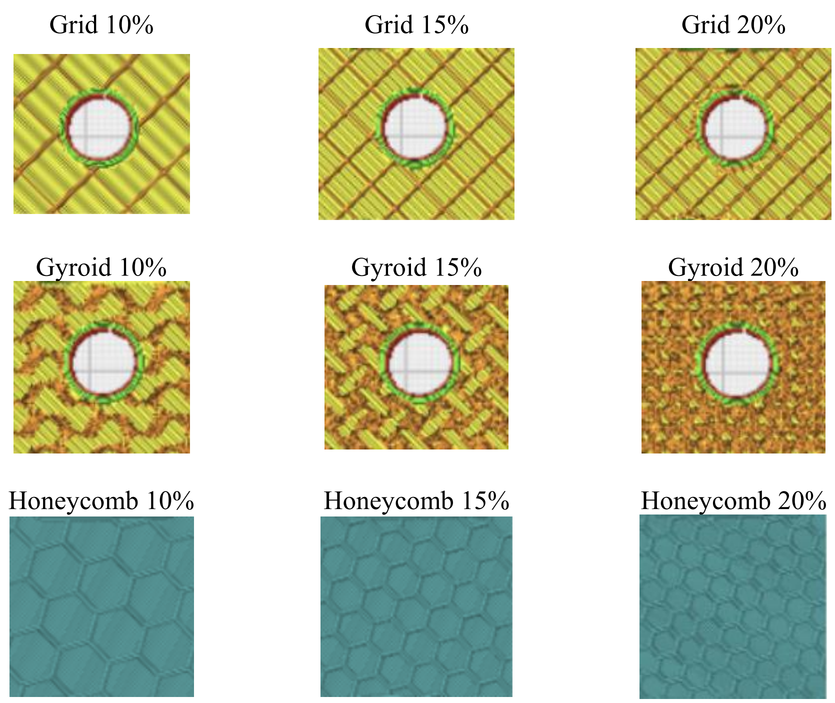

Fig. 1 Infill Patterns and Densities for Testing. Grid and Gyroid were sliced through UltiMaker Cura, and Honeycomb was sliced through PrusaSlicer.

IV. Experimental Test Methodology

A. Design Load

The Schrenk method is a simple analytical method used in preliminary aircraft design to estimate the lift force distribution on wings, proposed by Oster Schrenk [14]. The method is only applicable to unswept wings, especially on rectangular wings [14]. The method approximates the lift distribution by taking the average of the lift the unit span between elliptical lift and planform lift distribution. The mathematical models of the Schrenk method are as follows:

$$L'_{Schrenk} = \frac{L'_{elliptical} + L'_{planform}}{2} \tag{2}$$

$$L'_{elliptical} = \frac{4W}{\pi b}\sqrt{1-\left(\frac{2y}{b}\right)^2} \tag{3}$$

$$L'_{planform} = \frac{2W}{(1+\lambda)b}\left(1+\frac{2y}{b}(\lambda-1)\right) \tag{4}$$

Table 4 Properties of the Aircraft

Parameter	Value
Length of the Semi-Spanwise	30 in
Chord root	12 in
Chord tip	12 in
Weight of the aircraft	4.75 lb

To ensure the wing is capable of generating the required lift, the calculations include an extreme banking angle of 60 degrees and a factor of safety of 2, respectively. The half wingspan was divided into 100 sections and calculated using Eq. 3. and Eq. 4. Hence, the lift distribution, shear force, and bending moment diagrams along the wingspan are created and displayed in Fig.2, 3, and 4.

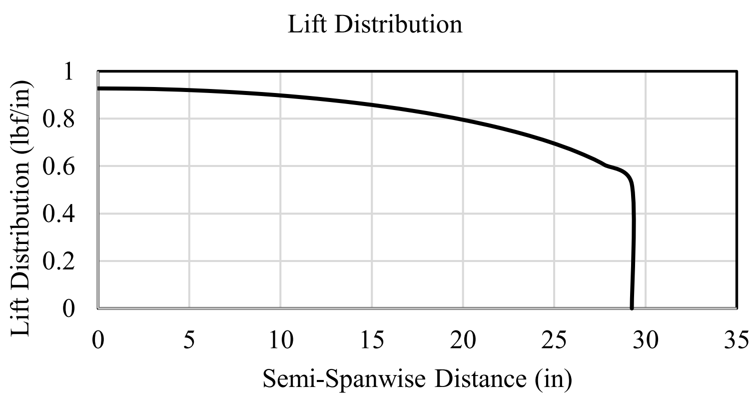

Fig. 2 Lift Force Distribution Based on Schrenk Method

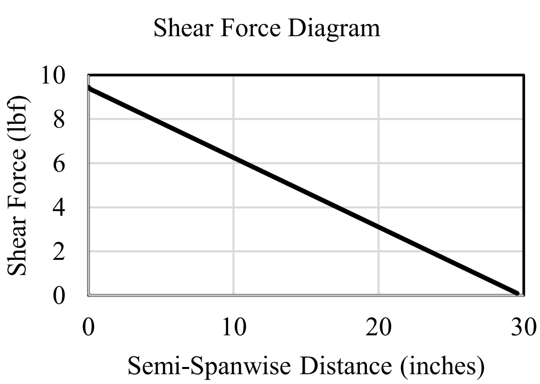

Fig. 3 Shear Diagram Based on Schrenk Method

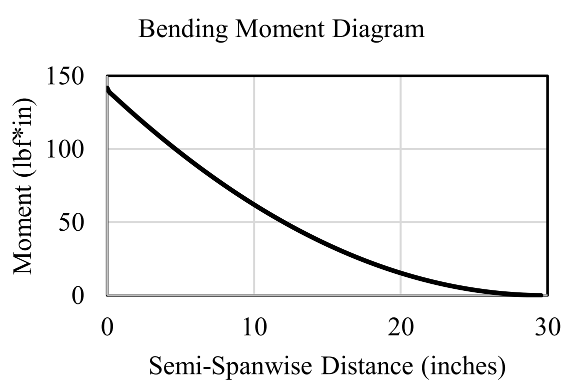

Fig. 4 Moment Diagram Based on Schrenk Method

From Fig. 3 and 4, the wingspan experiences the most load near the fuselage. Calculations were completed to ensure aircraft safety. The shape of the airfoil is irregular, which makes the calculation difficult. To assess such an obstacle. Another assumption was made to better evaluate the distance from the centroidal neutral axis to the extreme outer fiber and the second moment of area of the cross-section [15]. The vacancies in the wing rib were measured using the online CAD program Onshape [16].

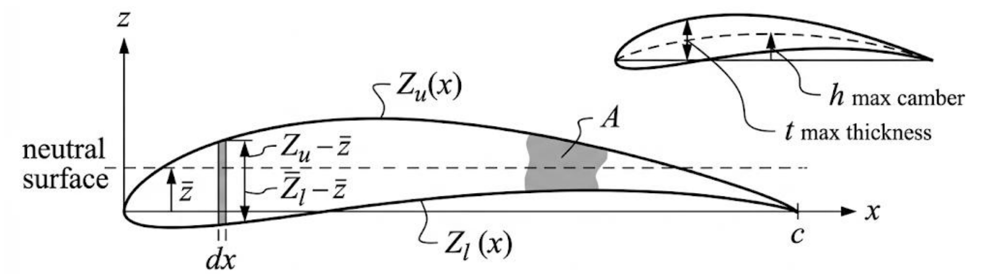

Fig. 5 Quantities for Determining and Estimating the Bending Inertia of an Airfoil Section [15]

The corresponding equations are provided below:

$$A = \int_0^c (Z_u - Z_l)\, dx \tag{5}$$

$$\bar{z} = \frac{1}{A}\int_0^c \frac{1}{2}\left(Z_u{}^2 - Z_l{}^2\right) dx \tag{6}$$

$$I = \int_0^c \frac{1}{3}\left[(Z_u - \bar{z})^3 - (Z_l - \bar{z})^3\right] dx \tag{7}$$

The calculations of the area, and neutral axis for the NACA 2412 profiled wing were carried out by exporting the data from the public database [5]. Using Eq. 6 and Eq. 7, a set data was imported to Microsoft Excel, and it's displayed in Fig. 6 In the dataset divide the airfoil into two sections: upper layer and lower layer. Utilized the trendline function in Excel to generate two functions for the two layers. Fig. 6 shows the neutral axis of the wing rib where the specimen is under zero stress and strain.

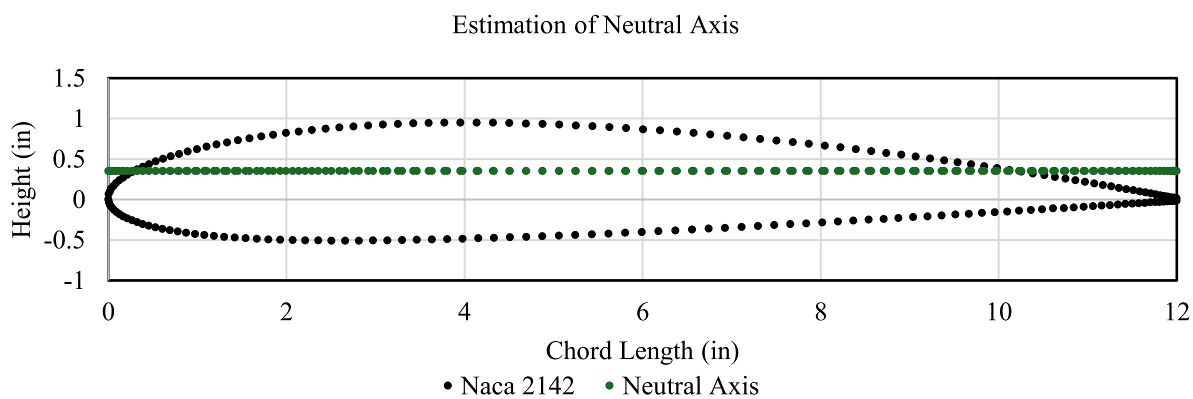

Fig. 6 Naca 2412 Airfoil Geometry

B. Test Setup and Experimental Procedure

A 3-point bend test was used to evaluate whether the wing rib experiences failure or deforms. An experiment test will be conducted in which a simulated lift force is applied on the rib for a set duration. The wing rib will be visually inspected to assess any signs of structural failures or deformation. This experiment used 3 sets of the same 3D-printed wing ribs of varying infill patterns and infill percentages.

To set up the test, the wing rib will be positioned upside down with both spars through their corresponding holes. An additional set of wing ribs, not used for testing, will be used as alignment guides for the spars so the specimen does not pinch or spread apart during loading, which could cause internal forces to occur. The spars will be supported on both ends while the test rib remains free-floating. Adequate clearance will be needed below to hang the maximum possible weight at the location of high pressure that could be experienced.

Fig. 7 Wing Rib Test Stand

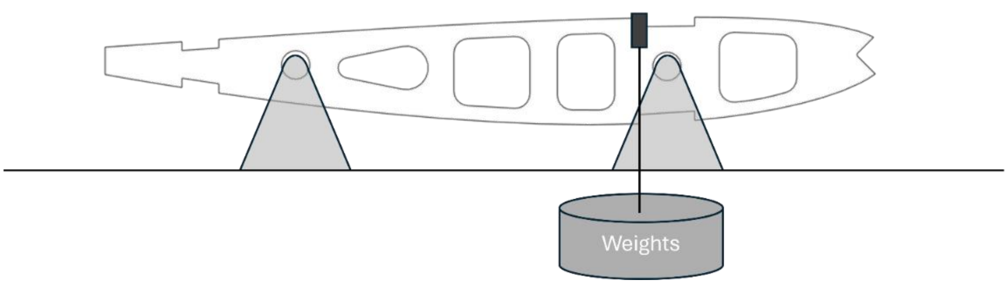

Fig. 8 Schematic of the 3-Point Bending Test

Once the experiment is set up, one wing rib from the set can be suspended on the spars, and the weights can be slowly added at the location of high pressure. Once the weight is on, start the timer for 2 minutes, which accounts for the two-180 and one 360-degree turns to ensure the structural integrity of the wing rib [2]. Once the time is over, remove the weight and inspect the rib for any failures or deformation. If the rib fails, stop and record the time of failure. Repeat the test for the remaining ribs of the same infill pattern and infill percentage to potential errors. Then repeat the test for the remaining types of infill patterns and infill percentages.

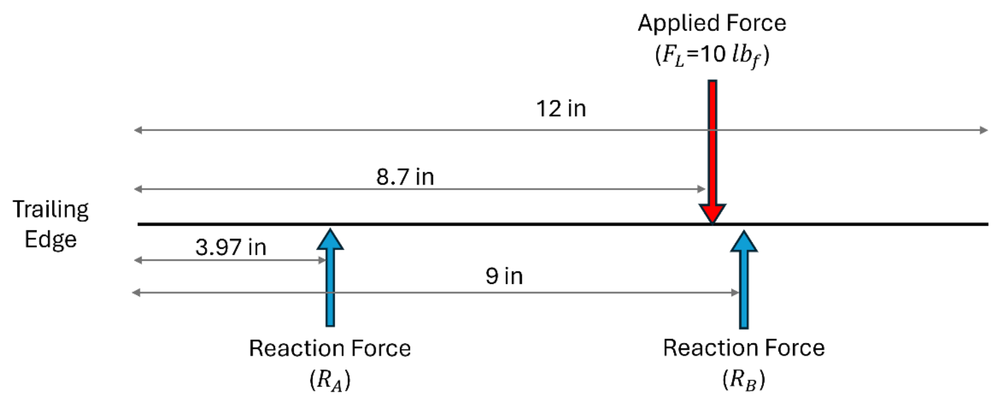

Fig. 9 Schematic of the Test Set-Up

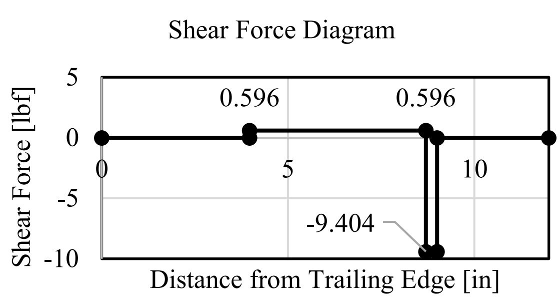

Fig. 10 Shear Force Diagram of the Specimen

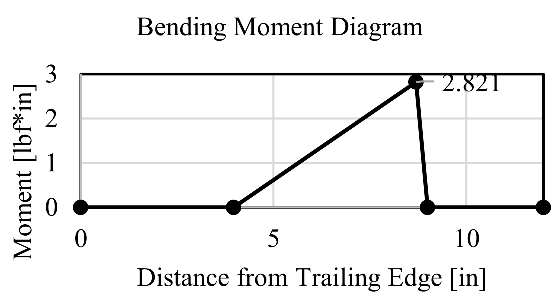

Fig. 11 Bending Moment Diagram of the Specimen

The spar is the main load-bearing member, which connects all the ribs and resists bending stress during flight. For a simple, solid airfoil, the bending stress at a point can be approximated using the equation:

$$\sigma = \frac{M_{max}c}{I} \qquad \text{Eq. (8)}$$

The maximum bending moment can be found from Fig. 11. The neutral axis was calculated using Eq. 8. Using the calculated data measures the distance between the neutral axis and the location of the applied load.

C. Evaluation

After the test, each wing rib was qualitatively evaluated through visual inspection. To clearly find any signs of deformation, the tested rib was stacked on an identical, untested rib for comparison, as shown in Fig.12. By aligning the tested rib on top of an untested rib, to serve as a control, any deformation or warping can be clearly seen or calibrated using this method. For all tested ribs, no visible deformation or failure occurred or was seen under the applied load.

Fig. 12 Wing Rib Comparison

V. Analysis & Discussion

D. Analysis

This study shows that the specific loading condition exhibits minimal structural response for the intended DBF application with varying structural behavior among the PLA specimens printed with different infill percentages and patterns. The evaluation focused on the location of the applied weight and observed that all the wing ribs sustained a 10-lb load for 2 minutes with no visible deformation or cracks. The bending stress acting on the aerodynamic center is 1.49 psi, which is low due to the high-pressure point being 0.3 in. away from the spar. The moment depends on the perpendicular distance from the pivot point to the line of action of the force. The measured bending stress is considerably lower than the material bending strength reported in Table 2, which validates the integrity of the structure.

Table 5 Comparison of 3D Print Time and Weight for Grid Infill Percentages

GRID			
Infill Percent	10%	15%	20%
3D Print Time	4 hr 17 min	4 hr 23 min	4 hr 31 min
Specimen 1 (oz)	0.6	0.65	0.63
Specimen 2 (oz)	0.6	0.62	0.65
Specimen 3 (oz)	0.59	0.62	0.64
Average (oz)	0.60	0.63	0.64

Table 6 Comparison of 3D Print Time and Weight for Gyroid Infill Percentages

GYROID			
Infill Percent	10%	15%	20%
3D Print Time	4 hr 25 min	4 hr 36 min	4 hr 49 min
Specimen 1 (oz)	0.57	0.64	0.64
Specimen 2 (oz)	0.59	0.64	0.65
Specimen 3 (oz)	0.58	0.63	0.65
Average (oz)	0.58	0.64	0.65

Table 7 Comparison of 3D Print Time and Weight for Honeycomb Infill Percentages

HONEYCOMB			
Infill Percent	10%	15%	20%
3D Print Time	5 hr 11 min	5 hr 28 min	5 hr 45 min
Specimen 1 (oz)	0.54	0.57	0.6
Specimen 2 (oz)	0.54	0.58	0.6
Specimen 3 (oz)	0.54	0.57	0.6
Average (oz)	0.54	0.57	0.60

From Table 5, Table 6, and Table 7, as infill percentages increase, the internal structure of the specimen becomes denser, strengthening the interlayer bonding, improving the mechanical properties of the specimen. However, increasing the infill percentage can reduce ductility and energy absorption capacity and may lead to stress concentration, which can be detrimental to the performance [17].

The different geometry can greatly impact the manufacturability and production process. The grid pattern is the most consistent and efficient out of all 3 patterns, with a print time of 4 hours 17 minutes at 10% infill. Conversely, the honeycomb pattern, due to the complexity of its hexagonal pattern, takes longer to print, increasing the time to 5 hours 11 minutes at 10% infill. The Gyroid is in between the two, offering a moderate print time of 4 hours 25 minutes at 10% infill.

For this year's DBF competition, the objectives involve carrying a payload and a banner, which can directly contribute to the total weight of the aircraft [2]. For an airfoil, the relationship between weight and lift is the primary driving force for performance. The table shows that the honeycomb pattern has the lightest weight out of the three patterns, with an average weight of 0.54 oz at 10% infill. While the grid pattern is the fastest to print, it is also the heaviest, averaging 0.60 oz at the same infill percentage compared to the honeycomb pattern. The gyroid is between the two, offering a moderate average weight of 0.58 oz at 10% infill.

E. Limitations

The ribs were tested under a worst-case scenario loading condition consisting of the maximum expected load of 10 pounds applied for a 2-minute duration. While this represents critical anticipated operating conditions, it does not account for repeated flights or load fluctuations. The test setup allowed controlled loading of the wing rib, but using a concentrated load limited the range of conditions that could be evaluated. A static load was chosen instead of simulating aerodynamic lift to simplify the experiment and focus on the rib's basic structural behavior since reproducing realistic flight forces would be difficult. Additionally, the rib was not attached to the full wing, which alters the load paths and stiffness. In addition, the supporting spars at both ends may not accurately simulate how spars behave when integrated into a full wing assembly. The test applied the load at the wing rib's quarter chord because this location corresponds to the aerodynamic center of the airfoil. All tested specimens were printed in the same X-Y orientation.

The evaluation of the tested ribs was qualitative through visual inspection; no deformations or defects were observed on any of the ribs. Although no failures were observed, visual inspection cannot detect internal defects such as cracks, separation of layers, or small elastic deformations that recover after unloading.

VI. Conclusion

Using the Schrenk method to approximate the lift distribution along the wingspan, the team verified the structural integrity of the wing rib using a three-point bend test. The results show that all infill percentages and patterns can withstand the calculated load. In this year's 2025-2026 DBF competition, the best infill percentage and pattern is the honeycomb pattern at 10% infill, which produces the lightest structure and prevents the addition of unnecessary weight to the aircraft while still withstanding aerodynamic load. Future work could expand on this study by incorporating fatigue testing through repeated loading cycles to evaluate how the ribs perform over multiple flights, ultimate load testing by gradually increasing loads until structural failure occurs and testing other print orientations to assess the structural integrity of various layer directions.

Acknowledgements

The authors would like to express sincere gratitude to our contributors who provided encouragement, guidance, and insightful feedback: Natania Middleton, Dr. Amir Hadadzadeh, Dr. Gladius Lewis, and Zuhanee Khan. We also acknowledge the support of Herff College of Engineering and the Department of Mechanical Engineering for providing the necessary resources and facilities for us to conduct our research. Finally, we gratefully extend our appreciation to the University of Memphis Chapter of AIAA and the Engineering Student Council for their financial assistance.

References

[1] H. Liu and M. Yu, "Structural design and lightweight optimization of small UAV airframes," *Journal of Aerospace Engineering*, vol. 27, no. 5, p. 04014020, 2014, doi: 10.1061/(ASCE)AS.1943-5525.0000389.

[2] American Institute of Aeronautics and Astronautics, "Design/Build/Fly competition rules and mission description," 2025. [Online]. Available: https://aiaa.org/dbf/

[3] I. Gibson, D. W. Rosen, and B. Stucker, *Additive manufacturing technologies: 3D printing, rapid prototyping, and direct digital manufacturing*, 3rd ed. Springer, 2021.

[4] S. Gudmundsson, *General Aviation Aircraft Design: Applied Methods and Procedures*, 2nd ed. Oxford, United Kingdom: Elsevier, 2022.

[5] "NACA 4-Digit Airfoil Generator," Airfoil Tools. [Online]. Available: http://airfoiltools.com/airfoil/naca4digit?MNaca4DigitForm%5Bcamber%5D=2&MNaca4DigitForm%5Bposition%5D=40&MNaca4DigitForm%5Bthick%5D=12&MNaca4DigitForm%5BnumPoints%5D=200&MNaca4DigitForm%5BcosSpace%5D=0&MNaca4DigitForm%5BcosSpace%5D=1&MNaca4DigitForm%5BcloseTe%5D=0&yt0=Plot

[6] Data download," *Overture 3D Printing*, Version 5.1, Aug. 2024. [Online]. Available: https://overture3d.com/pages/download#tds

[7] *Simplify3D Software Filament Properties Table*, Simplify3D Software, Nov. 22, 2022. [Online]. Available: https://www.simplify3d.com/resources/materials-guide/properties-table/

[8] I. Wright, "The melt flow index in polymer 3D printing: A concise engineer's handbook," *Engineering.com*, Jan. 25, 2024. [Online]. Available: https://www.engineering.com/the-melt-flow-index-in-polymer-3d-printing-a-concise-engineers-handbook/

[9] H. Gonabadi, A. Yadav, and S. J. Bull, "The effect of processing parameters on the mechanical characteristics of PLA produced by a 3D FFF printer," *The International Journal of Advanced Manufacturing Technology*, Oct. 2, 2020. [Online]. Available: https://link.springer.com/article/10.1007/s00170-020-06138-4

[10] *Anycubic Kobra Max User Manual*, Anycubic, 2024. [Online]. Available: https://www.anycubic.com/SupportCenter/documentHandbook/38

[11] "UltiMaker Cura - Infill Settings," *UltiMaker*. [Online]. Available: https://support.ultimaker.com/s/article/1667411002588

[12] "Infill Patterns," *Prusa Research*, 2026. [Online]. Available: https://help.prusa3d.com/article/infill-patterns_177130

[13] M. Eryildiz, "The effects of infill patterns on the mechanical properties of 3D printed PLA parts fabricated by FDM," *Ukrainian Journal of Mechanical Engineering and Materials Science*, Mar. 15, 2021. [Online]. Available: https://science.lpnu.ua/ujmems/all-volumes-and-issues/volume-7-number-1-2-2021/effects-infill-patterns-mechanical-properties

[14] O. Schrenk, "A simple approximation method for obtaining the spanwise lift distribution," *The Aeronautical Journal*, vol. 45, no. 370, pp. 331-336, 1941

[15] Lab 11 Lecture Notes, "Wing Bending Calculations," Massachusetts Institute of Technology, Cambridge, MA, USA, Document beambend.pdf, Spring 2007–2008. Available: https://web.mit.edu/16.unified/www/archives%202007-2008/spring%20temps/psets/systems/beambend.pdf

[16] Onshape, cloud-native computer-aided design (CAD) software, PTC Inc., Boston, MA, USA. [Online]. Available: https://www.onshape.com/ [Accessed: Feb. 26, 2026].

[17] E. Vázquez-Silva, J. A. Pintado-Pintado, F. P. Moncayo-Matute, P. B. Torres-Jara, and D. P. Moya-Loaiza, "Effect of Infill Density on the Mechanical Properties of Natural Peek Processed by Additive Manufacturing," *Polymers*, vol. 17, no. 3, Art. 347, Jan. 2025, doi: 10.3390/polym17030347. :contentReference[oaicite:0]{index=0}